

KEPLER-11 IS A SOLAR TWIN: REVISING THE MASSES AND RADII OF BENCHMARK PLANETS VIA PRECISE STELLAR CHARACTERIZATION

MEGAN BEDELL,¹ JACOB L. BEAN,¹ JORGE MELÉNDEZ,² SEAN M. MILLS,¹ DANIEL C. FABRYCKY,¹ FABRÍCIO C. FREITAS,²
IVAN RAMÍREZ,³ MARTIN ASPLUND,⁴ FAN LIU,^{4,5} AND DAVID YONG⁴

¹*Department of Astronomy and Astrophysics, University of Chicago, 5640 S. Ellis Ave, Chicago, IL 60637, USA*

²*Departamento de Astronomia do IAG/USP, Universidade de São Paulo, Rua do Matão 1226, Cidade Universitária, 05508-900 São Paulo, SP, Brazil*

³*McDonald Observatory and Department of Astronomy, University of Texas at Austin, USA*

⁴*Research School of Astronomy and Astrophysics, Australian National University, Canberra, ACT 2611, Australia*

⁵*Lund Observatory, Department of Astronomy and Theoretical physics, Lund University, Box 43, SE-22100 Lund, Sweden*

ABSTRACT

The six planets of the Kepler-11 system are the archetypal example of a population of surprisingly low-density transiting planets revealed by the *Kepler* mission. We have determined the fundamental parameters and chemical composition of the Kepler-11 host star to unprecedented precision using an extremely high quality spectrum from Keck-HIRES ($R \simeq 67,000$, S/N per pixel $\simeq 260$ at 600 nm). Contrary to previously published results, our spectroscopic constraints indicate that Kepler-11 is a young main-sequence solar twin. The revised stellar parameters raise the densities of the Kepler-11 planets by about 30%, making them more typical of the emerging class of “puffy” close-in exoplanets. We obtain photospheric abundances of 22 elements and find that Kepler-11 has an abundance pattern similar to that of the Sun with a slightly higher overall metallicity. We additionally analyze the *Kepler* lightcurves using a photodynamical model and discuss the tension between spectroscopic and transit/TTV-based stellar density estimates.

Keywords: stars: abundances, stars: fundamental parameters, techniques: spectroscopic, planets and satellites: fundamental parameters

1. INTRODUCTION

Five years after their initial discovery, the six planets of the Kepler-11 system remain a crown jewel of *Kepler* science results (Lissauer et al. 2011, hereafter L11). All six planets orbit a Sun-like host star with low eccentricities in a largely co-planar, tightly packed configuration. The formation and long-term stability of the system remains an open question (see e.g. Ikoma & Hori 2012; Hands et al. 2014; Mahajan & Wu 2014). Kepler-11 is regarded as the prototypical example of a system of tightly-packed inner planets, a class of *Kepler* multi-planet systems which offers a surprising counterpoint to our own solar system’s more widely spaced architecture. Given the low geometric probability of finding a six-planet transiting system, Kepler-11 is a valuable and rare opportunity to study in detail a potentially common population of exoplanets.

In addition to their unusually tight system architecture, the Kepler-11 planets are noteworthy in another sense: their measured masses and radii place them among the lowest-density super-Earths known to date. Transit timing variations (TTVs) have been measured for all six planets. In the discovery paper, L11 derived mass constraints for the five inner planets based on TTVs from six quarters of *Kepler* data. Migaszewski et al. (2012) reanalyzed the same data using a photodynamical model and found similar results, with an additional constraint on the outermost planet’s mass. The system was later revisited by Lissauer et al. (2013, hereafter L13) using fourteen quarters of *Kepler* data. All three analyses estimate mean densities of $\leq 0.5 \rho_{\oplus}$ for all the planets in the system, implying a considerable gas envelope on even the smaller super-Earths. This result has implications for potential formation scenarios, with the viability of forming such low-density planets on short orbits in situ up for debate (e.g. Lopez et al. 2012; Chiang & Laughlin 2013; Bodenheimer & Lissauer 2014; Howe & Burrows 2015).

Mean planet densities derived from transits and TTVs (or from transits and radial velocities) have a strong dependence on the assumed properties of the host star. Since the transit depth observationally constrains the ratio of planetary radius to stellar radius, the planet volume depends on the assumed stellar radius to the third power. The planet mass found from TTV inversion is correlated with the stellar mass. Host star characterization is therefore a critical part of measuring planet densities.

In past works, Kepler-11 has been characterized only through spectroscopic analysis of low to modest signal-to-noise data. Rowe et al. (2014), L11, and L13 all use moderate signal-to-noise ratio spectra ($S/N \leq 40$) from

Keck and apply the Spectroscopy Made Easy package (SME, Valenti & Piskunov 1996) to perform synthetic spectral fitting. The resulting stellar atmospheric parameters, when compared with stellar evolution models, indicate that Kepler-11 is a slightly evolved solar analog with a density of $0.80 \pm 0.04 \rho_{\odot}$ (L13). **Asteroseismic oscillation signals are not detected for Kepler-11, so the stellar density has not been independently determined (Campante et al. 2014).** Previous analysis of the stellar composition is also minimal. Adibekyan et al. (2012a) perform an equivalent width (EW) analysis on one of these Keck spectra to derive abundances of three α -elements and find that Kepler-11 has moderately low abundances of Ca, Cr, and Ti; however, the line list employed is quite limited with ≤ 5 lines per element.

Kepler-11’s well-characterized planetary system makes it a prime target for more detailed spectroscopic study. In this work, we present an analysis of a new, very high S/N spectrum. We use equivalent widths to measure the stellar properties and abundances of 22 elements at high precision.

The data are presented in Section 2. Derivation of the fundamental stellar properties from the spectrum is presented in Sections 3 and 4, and photospheric abundances are found in Section 5. We then present a new analysis of the *Kepler* lightcurve using a photodynamical model in Section 6. Finally, we compare the results from the spectroscopic and transit-based methods and discuss implications for the planetary system in Section 7.

2. DATA

Owing to its relative faintness ($V = 14.2$, L11), previous observations of Kepler-11 were at a signal-to-noise ratio insufficient for high-precision spectroscopic characterization. We dedicated nearly 8 hours of NASA-awarded Keck I time to obtaining a higher quality spectrum. Over the course of two consecutive nights (July 26-27 2015), we made 22 1200-s exposures of Kepler-11 for a co-added result of $S/N \simeq 260$ per pixel in the continuum near 600 nm. For these observations, HIRES was used with the B2 slit and kv387 filter, yielding a resolution $R \simeq 67,000$ and wavelength coverage between 390 and 830 nm.

We also observed the solar spectrum (via reflection from Ceres) and nine bright potential Kepler-11 twins with the same instrumental setup and similar S/N. The Kepler-11 twins were selected by imposing criteria of $5600 \leq T_{\text{eff}} \leq 5750$ K and $4.2 \leq \log g \leq 4.4$ dex on databases of previously published stellar parameters (Adibekyan et al. 2012b; Bensby et al. 2014). Preference

Table 1. Summary of derived fundamental stellar properties.

Spectrum	T_{eff} (K)	σ_T (K)	$\log g$ (dex)	$\sigma_{\log g}$ (dex)	v_t (km s ⁻¹)	σ_{v_t} (km s ⁻¹)	[Fe/H] (dex)	$\sigma_{[\text{Fe}/\text{H}]}$ (dex)
Sun (Ceres) ¹	5777		4.44		0.97		0.0	
K11	5836	7	4.44	0.02	0.98	0.02	0.062	0.007
HD1178	5650	7	4.36	0.02	0.93	0.02	0.013	0.008
HD10145	5637	16	4.39	0.05	0.87	0.04	-0.016	0.017
HD16623	5791	26	4.37	0.07	0.97	0.06	-0.462	0.022
HD20329	5606	7	4.38	0.02	0.88	0.02	-0.094	0.008
HD21727	5618	20	4.40	0.07	0.90	0.05	0.005	0.017
HD21774	5756	29	4.32	0.07	0.98	0.06	0.252	0.026
HD28474	5751	17	4.47	0.06	0.93	0.05	-0.614	0.014
HD176733	5609	9	4.41	0.03	0.87	0.02	-0.018	0.007
HD191069	5729	30	4.29	0.09	1.01	0.07	-0.033	0.025

¹Used as reference star.

was given to stars likely to be thick-disk members with approximately solar metallicity. These criteria were set based on the original spectroscopic analysis of Kepler-11 by L11, who found $T_{\text{eff}} = 5680 \pm 100$ K, $\log g = 4.3 \pm 0.2$ dex, $[\text{Fe}/\text{H}] = 0.0 \pm 0.1$ dex, and a significant chance of Kepler-11's being a thick disk member based on its kinematics.

The spectral extraction was performed by the Mauna Kea Echelle Extraction (MAKEE) pipeline.¹ All Kepler-11 spectra were then co-added using IRAF's *scombine*.² Continuum normalization was done by fitting low-order polynomial functions to each order, with care to use the same functional order for a given spectral order on every stellar spectrum to avoid bias in the subsequent differential analysis. Doppler corrections were applied using IRAF's *dopcor* task.

3. STELLAR PROPERTIES FROM SPECTROSCOPIC ANALYSIS

The fundamental properties of Kepler-11 and its potential twins were derived from an equivalent width analysis. We manually measured 94 Fe I and 17 Fe II spectral lines using IRAF's *splot*. The line list used unblended and unsaturated iron lines adapted from previous works such as Ramírez et al. (2014). Laboratory values for transition probability were adopted where available, but for this strictly differential analysis the values of $\log gf$

are largely irrelevant, since they cancel out for all lines in the linear region of the curve-of-growth. Equivalent widths were measured by carefully choosing local continua as described in Bedell et al. (2014) to maximize differential precision between the spectra. The full line list and measured equivalent widths are available in Table 3.

The stellar effective temperature T_{eff} , surface gravity $\log g$, metallicity $[\text{M}/\text{H}]$, and microturbulence v_t were determined by imposing a set of requirements on the iron abundances derived by MOOG (Snedden 1973). Namely, we required the $[\text{Fe}/\text{H}]$ abundances from both ionization states to be equal, and any trends in iron abundance with the excitation potential or reduced equivalent width of the lines to be minimized. As the most readily observable abundant metal in the photosphere, we used iron abundance $[\text{Fe}/\text{H}]$ as a direct proxy for metallicity $[\text{M}/\text{H}]$. It is important to note that we exclusively used the *differential* abundance measurements relative to the solar spectrum for this analysis. By directly comparing line-by-line differential abundances of spectrally similar stars, we minimize the influence of stellar model systematics on the final parameters and abundances (see e.g. Ramírez et al. 2014).

Parameter solutions were found iteratively using the *q²* python package.³ Uncertainties were determined by propagating scatter among the measured line abundances as described in Epstein et al. (2010) and Bensby et al. (2014).

¹<http://www.astro.caltech.edu/~tb/makee/>²IRAF is distributed by the National Optical Astronomy Observatory, which is operated by the Association of Universities for Research in Astronomy (AURA) under cooperative agreement with the National Science Foundation.³<https://github.com/astroChasqui/q2>

The resulting stellar parameters for all observed stars are given in Table 1. The T_{eff} and $\log g$ for Kepler-11 are significantly higher than previously determined values. We find $T_{\text{eff}} = 5836 \pm 7$ K, $\log g = 4.44 \pm 0.02$ dex, and $[\text{Fe}/\text{H}] = 0.062 \pm 0.007$ dex, while L13, for example, find $T_{\text{eff}} = 5666 \pm 60$ K, $\log g = 4.28 \pm 0.07$ dex, and $[\text{Fe}/\text{H}] = 0.00 \pm 0.04$ dex. Potential sources of this tension include the substantially different S/N of spectra used and the difference in analysis technique. L13 and other previous analyses use SME, which fits synthetic spectra to the observations. Different choices of spectral analysis technique have been shown to vary the derived stellar parameters beyond their nominal error estimates, so this explanation cannot be ruled out (Hinkel et al. 2016). However, since our analysis is performed relative to the solar spectrum, our results are anchored to the accurate stellar parameters of the Sun. Furthermore, our method is strictly differential, based on line-by-line comparison of equivalent widths measured using spectra of the Sun and Kepler-11 gathered with the same instrumentation and in the same observing run. Thus, our approach minimizes possible systematic errors that could affect other analyses.

Our revised stellar parameters securely place Kepler-11 in the solar twin category. This can be seen even by eye: as depicted in Figure 1, at high S/N Kepler-11’s spectrum is nearly identical to the solar spectrum and distinctly different from that of HD1178, the star from our sample whose fundamental parameters most closely match those found by L13. In particular, the solar-like $\log g$ for Kepler-11 implies that it is denser and less evolved than previously thought.

We used stellar evolutionary models to estimate the mass, radius, and age of Kepler-11. Yonsei-Yale isochrones were fit using q^2 (Figure 2). We also applied Dartmouth and Basti isochrones using the *isochrones* python package (Morton 2015). All three models gave results consistent within 1σ . From these fits, we estimate a stellar mass $M_{\star} = 1.040 \pm 0.006 M_{\odot}$, radius $R_{\star} = 1.008 \pm 0.024 R_{\odot}$, and age 3.2 ± 0.8 Gyr. This gives a stellar density $\rho_{\star} = 1.43 \pm 0.10 \text{ g cm}^{-3}$, or $1.01 \pm 0.07 \rho_{\odot}$.

4. ALTERNATIVE STELLAR AGE INDICATORS

We used several alternate methods to measure the age of Kepler-11 as an independent test of its evolutionary state. The results unanimously agree upon a sub-solar age for Kepler-11. Details of the methods used follow.

4.1. Stellar Rotation

The apparent rotation rate $v \sin i$ was measured using five saturated lines (Fe I 6027.050 Å, 6151.618 Å,

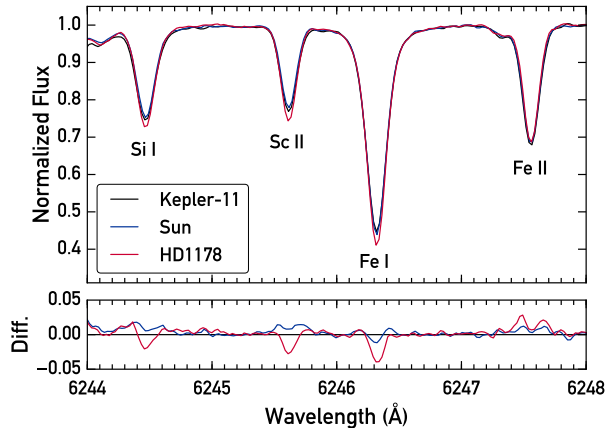


Figure 1. A small section of the Keck-HIRES spectra of the Sun (blue), Kepler-11 (black), and HD1178 (red), which has fundamental parameters similar to those given by Lissauer et al. (2013) for Kepler-11. Residuals for flux relative to the Kepler-11 spectrum are plotted in the lower panel.

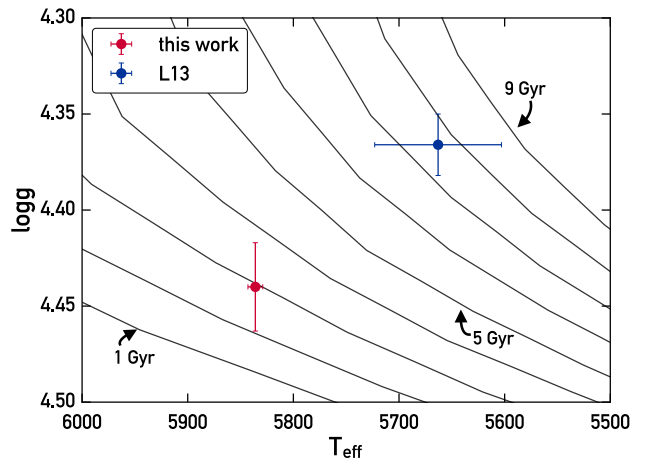


Figure 2. Measured stellar properties of Kepler-11 from this work and from L13 plotted with Yonsei-Yale isochrones at a metallicity of 0.06 dex.

6165.360 Å, 6705.102 Å, and Ni I 6767.772 Å) from the Keck spectrum. The procedure used is described in depth in dos Santos et al. (2016), and is summarized here. We first measured the macroturbulence value $v_{\text{macro},\odot}$ for each line in the solar reference spectrum using MOOG *synth* with $v \sin i_{\odot}$ fixed at 1.9 km s^{-1} . We then calculated v_{macro} for Kepler-11 using the measured solar values and an empirical relation given in Equation 1 of dos Santos et al. (2016) which calculates the expected v_{macro} difference from the Sun as a function of stellar T_{eff} and $\log g$. This relation was derived using 10 solar twins observed at very high resolution with HARPS, so we expect the v_{macro} relation to be accurate

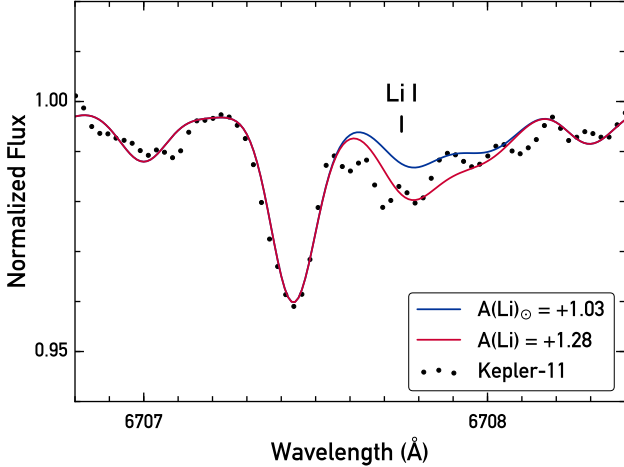


Figure 3. Observed spectrum of Kepler-11 around the Li I 6707.8 Å line. Synthetic fits for the best-fit Li abundance (red) and the solar Li abundance (blue) are overplotted.

for the solar twin Kepler-11 as well. Finally, MOOG *synth* was used to find $v \sin i$ for each line in Kepler-11’s spectrum with v_{macro} fixed to the calculated value.

The five lines give a consistent result of $v \sin i = 2.2 \pm 0.2 \text{ km s}^{-1}$. Assuming alignment of the stellar spin axis with the orbital axis of its transiting planets, we can take $v \sin i$ as the true rotational velocity. This translates to an age of 3.4 Gyr using the law of Skumanich (1972) anchored by the Sun, or 3.0 Gyr from dos Santos et al. (2016)’s updated relation.

4.2. Lithium Abundance

The lithium abundance of Kepler-11 was measured by synthesizing the Li I 6707.8 Å line with MOOG *synth*. The line list was adopted from Meléndez et al. (2012) and includes blends of atomic and molecular lines. We find a lithium abundance of $A(\text{Li}) = 1.28 \pm 0.07$, higher than the measured solar value of 1.03 ± 0.04 at the level of 3σ (Figure 3). After applying NLTE corrections, these values become $A(\text{Li}) = 1.32 \pm 0.07$ for Kepler-11 and $A(\text{Li})_{\odot} = 1.07 \pm 0.04$ for the Sun (Lind et al. 2009).⁴ Kepler-11’s higher lithium abundance implies a sub-solar age, since lithium is depleted throughout a star’s main-sequence lifetime (Duncan 1981). Using the solar-twin-based lithium-age relation from Carlos et al. (2016) gives an age estimate of about 3.5 ± 1.0 Gyr for Kepler-11.

4.3. [Y/Mg] Abundance Ratio

Recent works by Nissen (2015) and Tucci Maia et al. (2016) have identified the ratio of yttrium to magnesium abundances as an excellent proxy for age in main-sequence Sun-like stars. We measured these abundances as described in Section 5 and found a [Y/Mg] ratio of 0.04 ± 0.05 dex. Using the age relation from Tucci Maia et al. (2016), this gives an age of 4.0 ± 0.7 Gyr.

4.4. Chromospheric Emission

We measured the chromospheric emission level of Kepler-11 using the Ca II H line. Since our spectral coverage cut off around 390 nm at the blue end, it was not possible to obtain a measurement of the standard chromospheric activity index $\log(R'_{\text{HK}})$. Instead, we defined an alternative index H as the flux integrated from a 1.3 Å width triangular filter centered on the H line at 3968.47 Å, divided by the continuum integrated with a flat filter of 5 Å width around 3979.8 Å. This measurement of H was converted to the standard Mount Wilson S_{HK} using the following equation, which was derived from the literature values of ten Sun-like stars:

$$S_{\text{HK}} = 0.901H + 0.033 \quad (1)$$

We find an activity index $\log(R'_{\text{HK}}) = -4.82$. This is slightly higher than the maximum activity level of the solar cycle and suggests a sub-solar age (Skumanich 1972). The activity-age relation for solar twins given in Freitas et al. (2016) yields an age estimate of 1.7 Gyr, although this is quite uncertain since we have measured the activity level at only one epoch and cannot average over the activity cycle.

5. STELLAR ABUNDANCES

We measured photospheric abundances using the curve-of-growth technique for 20 other elements (excluding lithium, whose synthesis-based abundance determination is discussed in Section 4.2). As with the iron lines, all equivalent widths were measured by hand and line-by-line differential abundances determined with MOOG using q^2 . The line list was adapted from previous works including Bedell et al. (2014). For the element K, only one line was available, so it was measured multiple times and the deviation of the results was used as an error estimate; however, this uncertainty may be underestimated due to the line’s location near a telluric-contaminated region. Hyperfine structure corrections were applied for Co I, Cu I, Mn I, V I, and Y II following Meléndez et al. (2012). Non-LTE corrections were applied for O I using grids from Ramírez et al. (2007). Carbon abundances were measured by a combination of C I and CH lines; we note that the abundances

⁴Data obtained from the INSPECT database, version 1.0 (<http://www.inspect-stars.com>)

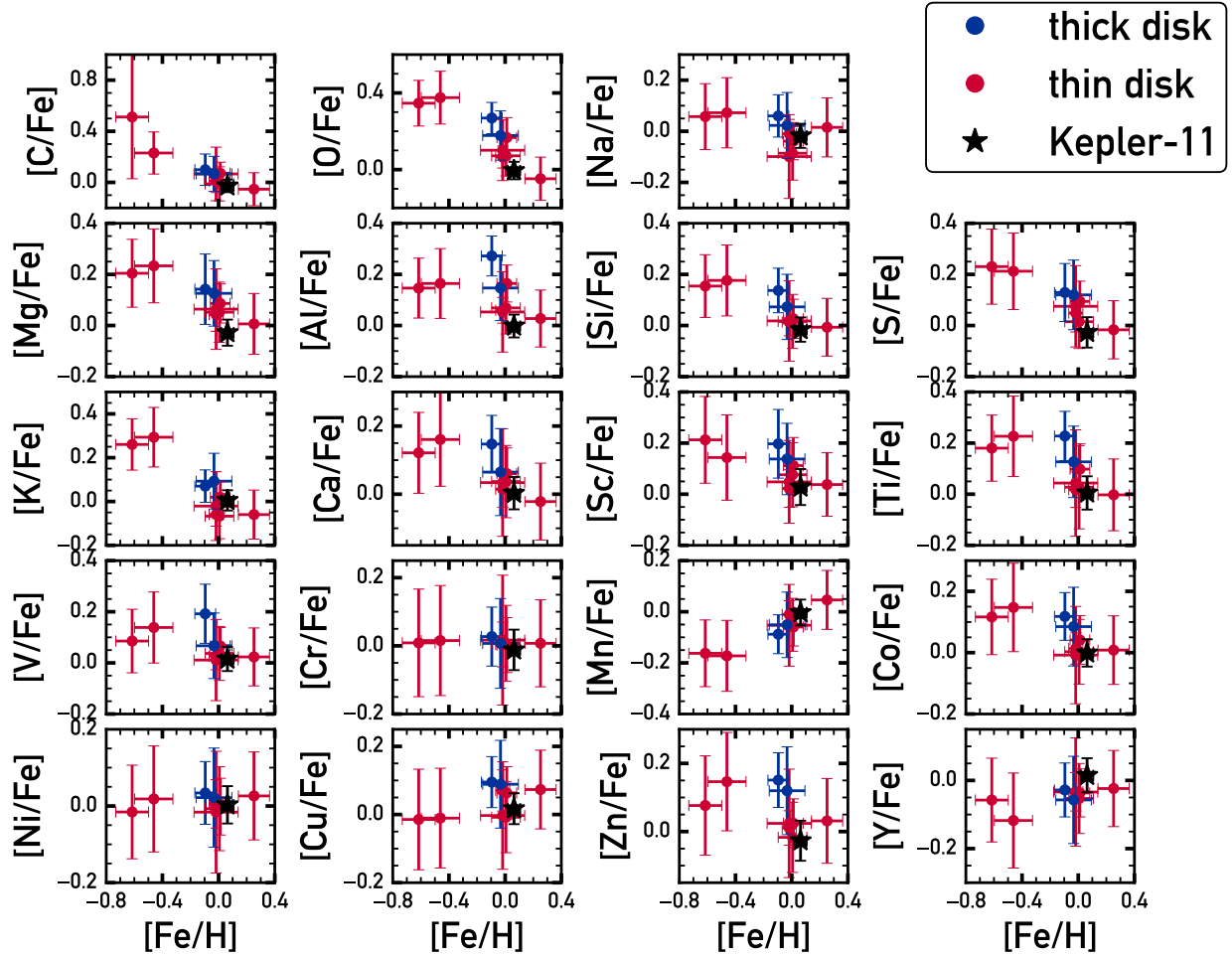


Figure 4. Measured abundances plotted as a function of metallicity for the full sample. Thin (red circle) and thick (blue circle) disk stars are categorized by their kinematic membership probabilities. Kepler-11 is represented as a black star.

for the two species are in tension at the $\sim 2\sigma$ level for several of the stars in the sample, indicating that there may be some systematic effects at play. The measured equivalent widths are given in Table 3, and resulting abundances for all stars are in Table 4. The quoted abundance errors include both the intrinsic scatter of the lines and the uncertainty propagated from errors on the stellar parameters. For subsequent analysis, all measured states of a given element (e.g. CI and CH, TiI and TiII, etc.) were combined with a weighted average to yield the overall elemental abundance.

Since Kepler-11 was previously thought to be a potential thick-disk member based on its low radial velocity ($RV = -57.16 \text{ km s}^{-1}$ in L11; we find $-56.7 \pm 0.7 \text{ km s}^{-1}$), several of the stars in the “twin” sample were selected by thick-disk kinematics. As a result, we have both thin and thick disk stars in our abundance sample. The detailed abundances of these groups can be quite

different even within a small range of metallicities (see e.g. Liu et al. 2016). In Figure 4, we plot the abundances for thick- and thin-disk stars as a function of their measured metallicity. Disk membership was assigned based on UVW kinematics using the procedure specified in Reddy et al. (2006).

Kepler-11 follows the abundance trends of the other thin-disk stars well and does not display a notable α -element enrichment. In fact, we find that despite its low radial velocity, its UVW kinematics are consistent with it being a thin disk member. Using the proper motions from UCAC3 (Zacharias et al. 2010), our measured RV, and the isochrone-based absolute magnitude estimate ($M_V = 4.7$ or a parallax of 1.3 mas), we find $(U, V, W) = (8.11, -43.71, -6.28) \text{ km s}^{-1}$. This translates to a 98% probability of Kepler-11 belonging to the thin disk population.

Kepler-11’s status as a thin-disk solar twin enables direct comparison of its abundance pattern to that of the Sun and other known solar twins. Of particular interest is the question of trends in elemental abundances with condensation temperature (T_C). As shown by Meléndez et al. (2009), the solar abundance pattern is unusual in its depletion of refractory elements relative to volatiles. This depletion has been interpreted as “missing” rocky material that is locked up in the Solar System planets (Chambers 2010). Building up the number of stars with precisely characterized abundance patterns and planetary systems can help to test this possibility.

We applied corrections for the effects of galactic chemical evolution (GCE), which can change the abundance patterns and T_C trends of stars at varying ages (Nissen 2015; Spina et al. 2016a). We corrected each abundance $[X/H]$ using the linear relationships found by Spina et al. (2016b), who fit $[X/H]$ as a function of stellar age for a sample of solar twins. We then used the corrected abundances and T_C values from Table 8 of Lodders (2003) to search for a trend.

The uncertainty on the trend of $[X/H]$ with T_C was propagated using a bootstrap Monte Carlo method to account for multiple potential sources of error. Each abundance is uncertain due to the intrinsic scatter of abundances derived from different lines. This uncertainty increases when the GCE correction is applied, since the correction coefficients carry some degree of random error. Additionally, the slope of the T_C trend can be altered by errors on the fundamental stellar parameters used (as seen in Teske et al. 2015) and by the uncertainty on stellar age in the GCE correction. We account for all of these effects by running 10,000 bootstrap trials where the stellar parameters are resampled from their posterior distributions; the resulting abundances are randomized by drawing samples from the multiple measured lines; the age is determined based on the resampled stellar parameters; and the GCE correction is applied using coefficients that have been randomly sampled from the (assumed Gaussian) uncertainties given in Spina et al. (2016b). The resulting distribution of T_C trend fits gives a slope of $[X/H]$ vs T_C of $(-4.6^{+7.9}_{-8.7}) \times 10^{-6}$ dex K^{-1} (Figure 5). In short, the trend of Kepler-11’s abundances with T_C is indistinguishable from the solar pattern, albeit with a large degree of uncertainty due to the many sources of error which come into play when considering GCE effects.

6. STELLAR PROPERTIES FROM PHOTODYNAMIC TRANSIT ANALYSIS

6.1. Analysis

In order to reassess the stellar density constraint based on the transit data, we performed a photodynamical fit to the full *Kepler* short cadence (58.8 second exposure) data set. The model integrates the 7-body Newtonian equations of motions for the central star and six planets, including the light-travel-time effect. When the planets pass between the star and the line of sight, a synthetic light curve is generated (Pál 2012), which can then be compared to the data. This approach therefore takes into account all transit-timing variations, simultaneously constraining planet masses, eccentricities, and radii. To prepare the data for fitting, we detrended the data with a cubic polynomial with a 2880 minute (2 day) width every 100 points, and interpolated for points between. We divided the flux by this fit as a baseline to generate our data set of 1746779 points. We additionally multiplied the uncertainties given by *Kepler* by a factor of 1.115318 so that the reduced χ^2 of a fiducial model was 1.0. This broadens our posteriors and helps take into account unmodeled noise in the data. To simultaneously generate the posteriors on all of our model parameters, we ran differential evolution Markov chain Monte Carlo (DEMC-MC, Ter Braak 2005) fits with planetary parameters $\{P, T_0, e^{1/2} \cos(\omega), e^{1/2} \sin(\omega), i, \Omega, R_p/R_\star, M_p/M_\star\}$ for all planets, where P is the period, T_0 is the mid-transit time, e is eccentricity, ω is the argument of periape, i is inclination, Ω is nodal angle, and R and M are radius and mass, respectively (with subscripts p = b, c, d, e, f, g for the planets and \star for the star). The star has five additional parameters: $\{M_\star, R_\star, c_1, c_2, dilute\}$, where $\{c_i\}$ are the two quadratic limb-darkening coefficients and $dilute$ is the amount of dilution from other nearby sources. We used eccentricity vector components scaling as $e^{1/2}$ so that we get flat priors in total e , and fixed the values of $dilute = 0$ since there is no evidence of other nearby stars diluting the lightcurve. We also fixed the value of M_\star , as transits alone generally only give information about the density of the star, rather than M_\star and R_\star individually. We fixed $\Omega = 0$ for all planets because the data are not precise enough to constrain these values (Migaszewski et al. 2012). Additionally, it is extremely unlikely that there are large mutual inclinations among the planets given that we see six transiting planets (L11, Figure 4), five of which are dynamically packed and thus have no misaligned non-transiting planets between them (L11). We used flat priors for all other parameters.

We ran two DEMCMCs to model the data. One had no constraints on the stellar radius, i.e., allowed the transits themselves to completely determine the stellar density, which we will label \mathcal{NST} for “No Spec-

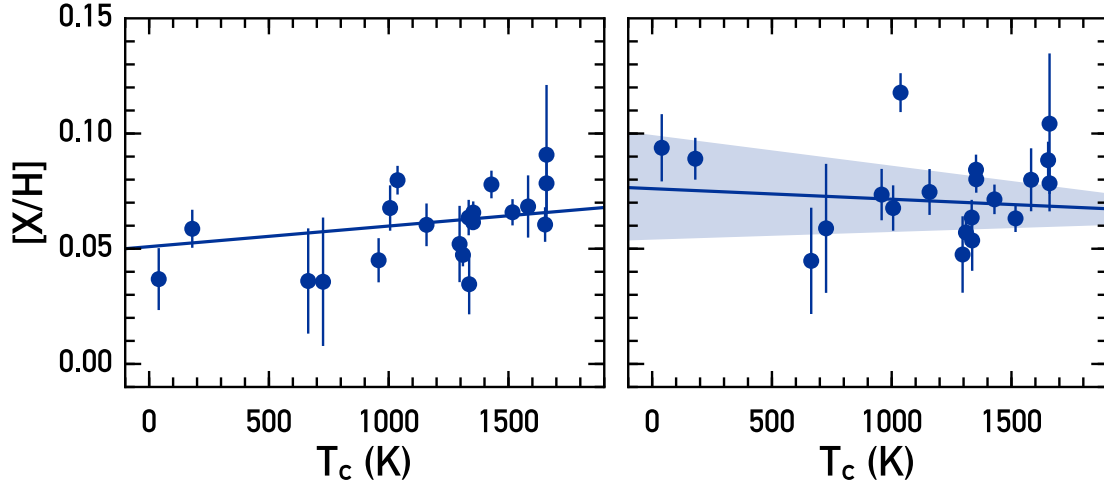


Figure 5. Abundances of Kepler-11 relative to the Sun as a function of the condensation temperature of the element within the protoplanetary disk. Error bars on the abundances come from the line-to-line scatter only (that is, not including systematic errors from the stellar parameters). Left panel shows the abundances and best-fit linear trend before applying galactic chemical evolution (GCE) corrections. In the right panel, the data have been GCE-corrected following [Spina et al. \(2016b\)](#), assuming a stellar age of 2.7 Gyr, with error bars from the line-to-line scatter and propagated uncertainty in the stellar age. The shaded region represents the 1σ uncertainty interval on the linear fit to $[X/H]$ vs T_c from the bootstrap simulation described in the text.

tral Information.” The second DEMCMC was run with the stellar mass and radius fixed at the spectroscopically measured values in this study, $M_\star = 1.04M_\odot$ and $R_\star = 1.00M_\odot$, which we will label *FSP* for “Fixed Stellar Parameters.” The *NSI* run produces a lower density star $\rho_\star = 1.191^{+0.043}_{-0.11} \text{ g cm}^{-3}$ than the fixed value of $\rho_\star = 1.466 \text{ g cm}^{-3}$ in *FSP*. This indicates that the transit data alone are discrepant with the spectroscopically measured stellar density. Table 2 shows the density results for all bodies for both DEMCMC runs. We note that the densities of planets with no spectral information, *NSI*, are slightly higher than reported in L13 because that study includes the lower spectroscopically measured stellar density in their final best fits.

The best fit solution from *NSI* run has a lower χ^2 value by more than 40 compared to the best-fit *FSP* run. Thus we see that fixing the stellar parameters at their spectroscopically measured values causes the fit to the *Kepler* data to become significantly worse; the p-value for such an increase in χ^2 is on order 10^{-9} . This confirms the existence of tension between the transit measured stellar density and the spectroscopically measured one.

6.2. Physical Interpretation

Transit measurements of stellar (and thus planet) densities rely on the the transit of the planet probing the width of the star. For a given stellar mass, once the

period of a planet is known from successive transits its orbital velocity (v_{orb}) can be determined. The physical distance a planet traverses during the duration of a transit (T_{dur}) is to a very good approximation $T_{\text{dur}}/v_{\text{orb}}$. There are two main degeneracies between the stellar radius and the measured duration: (1) eccentricity of the planets orbit and (2) impact parameter of the transit.

Eccentricity changes v_{orb} as a function of orbital phase following Kepler’s Second Law. However the observed transit timing variations provide information on the level of eccentricity of the interacting planets, and they are all found to be very small (< 0.05), only negligibly affecting the measured stellar radius. Using standard orbital mechanics, it may be seen that $\rho_\star \propto R_\star^{-3} \propto v_{\text{orb}}^{-1} = (GM_\star(\frac{2}{r} - \frac{1}{a}))^{-1/2} \propto 1 - e \sin \omega + \mathcal{O}(e^2)$, where G is the Newtonian gravitational constant, a is the planet’s semi-major axis, and r is the instantaneous star-planet distance. Thus a change in ρ_\star by the $\sim 20\%$ required to reconcile the spectroscopic and TTV measurements would require a uniform increase in $e \sin \omega$ across all planets of order 0.06, well beyond that allowed by the TTVs. Our fits marginalize over the range of possible eccentricities by including the eccentricity vectors as free parameters when fitting for stellar and planetary densities. In the *FSP* DEMCMC, the planets’ eccentricities do increase substantially, but the chains are unable to find a TTV solution nearly as good as for the low eccentricity case, as discussed above.

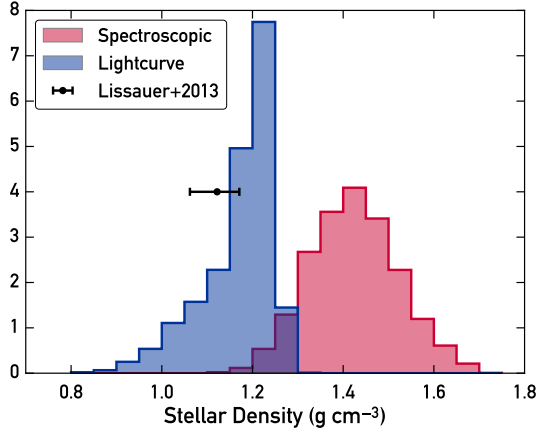


Figure 6. Posterior distributions for the stellar density from isochrone fits to the spectroscopic parameters (red) and from photodynamical modeling of the lightcurve (blue). The TTV-based stellar density from L13 is also plotted with one-sigma errors for comparison (black).

The second major degeneracy (impact parameter, b) is determined by the shape of the transits. The slope of the ingress/egress indicates the curvature of the star during ingress/egress and therefore the radius of the star may be computed via $R_\star = (a/b) \cos i$, where a is the semi-major axis and i is the inclination. We also marginalize over these parameters, but note that the impact parameter is a positive definite quantity, and is consistent with 0 for planets d and g. Without perfectly measured transit shapes, there is some freedom to increase impact parameter away from 0 simultaneously with an increase in stellar radius so that the transit chord and thus T_{dur} is constant. If the stellar radius is decreased while the impact parameter is at or near 0, then there is no such compensatory degenerate parameter to change that would increase the transit chord, and the well-measured value of T_{dur} no longer fits the model. This results in the asymmetric photodynamically measured stellar density as shown in Fig. 6.

We also consider the effects of potential star spot crossing changing the apparent TTVs or transit durations. If star spots variations were contributing significantly to the fits, we would expect to see a greater reduced χ^2 in transit compared to out of transit, as our transit model would not properly fit the planets’ transits over star spots or faculae. This effect is not observed, strengthening our confidence in the sufficiency of our model.

7. DISCUSSION

7.1. Discrepancies in Stellar Densities

The stellar densities found through spectroscopic characterization ($1.43 \pm 0.10 \text{ g cm}^{-3}$) and photodynamical modeling ($1.191^{+0.043}_{-0.11} \text{ g cm}^{-3}$) are inconsistent at the level of $\geq 2\sigma$ (Figure 6). The uncertainties on the fundamental stellar parameters would need to have been underestimated by at least a factor of 4 to allow 1- σ agreement with the lightcurve-based stellar density measurement, which we regard as unlikely from extensive tests on our spectroscopic methods (Bedell et al. 2014; Ramírez et al. 2014). While stellar densities from fundamental parameters can be strongly dependent on imperfect stellar isochrone models, we note that in this case Kepler-11’s extreme similarity to the Sun places it near the anchor point of most models, increasing the accuracy of isochronal analysis. Moreover, multiple independent age determination methods support the result of a young, non-evolved age and therefore a solar-like density for Kepler-11.

An alternative hypothesis is that some bias in the transit analysis has resulted in an erroneously low inferred stellar density. As described by Kipping (2014), multiple effects can bias the density measured by transits, including stellar activity, blended background sources, and non-zero planet eccentricities. Bias due to an underestimated planet eccentricity is not a likely explanation in this case, since all five planets give a consistent stellar density. Also, the photodynamical modeling used in this analysis should be robust to the effects of transit timing or duration variations on the measured stellar density. This leaves two potentially viable explanations from Kipping (2014) for the density discrepancy: stellar activity (the “photospot” effect) or a background source (the “photoblend” effect).

Starspots effectively reduce the observed stellar flux, artificially raising stellar density inferred from the transit depth, which is the opposite of the effect we seek to explain. However, as a $\sim 3\text{--}4$ Gyr Sun-like star, Kepler-11’s activity may manifest mostly in the form of plages (Radick et al. 1998). Unocculted plages could potentially lower the observed stellar density by inflating the measured radii (Oshagh et al. 2014). Given the observed behavior of other main-sequence solar analogs and the lack of rotational modulation in the *Kepler* lightcurve, the filling factor for spots or plages on Kepler-11’s surface should be of order a few percent at most (Meunier et al. 2010). This would yield a similarly small percent-level change in the observed stellar density (Kipping 2014). Furthermore, the active region configuration would need to be relatively stable throughout *Kepler*’s four years of observations, which is unlikely at the high level of activity needed to have a large plage filling factor.

Table 2. Star and Planet Densities

Body	\mathcal{NST}			\mathcal{FSP}		
	Mass (M_{\oplus})	Radius (R_{\oplus})	Density (g cm^{-3})	Mass (M_{\oplus})	Radius (R_{\oplus})	Density (g cm^{-3})
Kepler-11 b	$2.78^{+0.64}_{-0.66}$	$1.83^{+0.07}_{-0.04}$	$2.45^{+0.63}_{-0.62}$	$2.83^{+0.62}_{-0.66}$	$1.71^{+0.02}_{-0.02}$	$3.15^{+0.70}_{-0.74}$
Kepler-11 c	$5.00^{+1.30}_{-1.35}$	$2.89^{+0.12}_{-0.04}$	$1.11^{+0.32}_{-0.32}$	$5.05^{+1.19}_{-1.37}$	$2.694^{+0.019}_{-0.019}$	$1.43^{+0.34}_{-0.39}$
Kepler-11 d	$8.13^{+0.67}_{-0.66}$	$3.21^{+0.12}_{-0.04}$	$1.33^{+0.14}_{-0.15}$	$7.52^{+0.68}_{-0.68}$	$3.000^{+0.017}_{-0.017}$	$1.54^{+0.14}_{-0.14}$
Kepler-11 e	$9.48^{+0.86}_{-0.88}$	$4.26^{+0.16}_{-0.07}$	$0.664^{+0.079}_{-0.087}$	$8.37^{+1.01}_{-1.04}$	$3.947^{+0.024}_{-0.024}$	$0.750^{+0.091}_{-0.093}$
Kepler-11 f	$2.53^{+0.49}_{-0.45}$	$2.54^{+0.10}_{-0.04}$	$0.83^{+0.18}_{-0.16}$	$1.59^{+0.58}_{-0.54}$	$2.356^{+0.028}_{-0.028}$	$0.67^{+0.24}_{-0.23}$
Kepler-11 g	< 27	$3.33^{+0.26}_{-0.09}$	< 4	< 29	$3.099^{+0.027}_{-0.026}$	< 5
Kepler-11	$\rho_{\star} = 1.194^{+0.042}_{-0.11} \text{ g cm}^{-3}$			$\rho_{\star} = 1.466 \text{ g cm}^{-3}$ (fixed)		

NOTE—Medians and 1- σ uncertainties from the DEMCMC runs as described in § 6

The final effect is blending of unresolved background sources, which can cause stellar density to be underestimated. Recently Wang et al. (2015) found two visual companions to Kepler-11 at separations of 1.36" and 4.9" using AO imaging. With brightness differences of $\Delta K = 4.4$ mag and 4.7 mag respectively, these companions should contribute approximately 3% of the total flux in the Kepler bandpass. Using Equation 9 of Kipping (2014), this implies that the observed stellar density from transits should be $\sim 99\%$ of the true density. The known companions are therefore insufficient to explain the magnitude of the density discrepancy.

We are left with no obvious culprit for the discrepancy between the stellar densities measured from spectroscopic characterization and lightcurve modeling. Similar testing for other systems with measured TTVs is an important next step in determining whether this is a one-off event due to, e.g. underestimated uncertainties of stellar properties or unexpected stellar activity in the lightcurve, or if it is a systematic difference between these independent methods of analysis. **If this is a systematic effect, it may be linked to the mass underestimation problem in TTV measurements relative to RVs found by Weiss & Marcy (2014).**

7.2. Implications for the Planets

The adopted mass and radius of Kepler-11 has considerable repercussions for its planetary system. We can approximate the planet mass derived from TTVs as a linear function of the assumed stellar mass. The planet radius also has a linear dependence on stellar radius, since only the relative surface areas of planet and star can be measured by the transit depth. The stellar properties obtained through spectroscopic analysis therefore **raise the planet masses by 8% and lower the planet radii by 5%** relative to the transit and TTV-derived values. The results are shown in Figure 7.

Adopting the stellar properties from spectroscopic analysis raises the mean densities of the Kepler-11 planets by $\sim 30\%$. These increased densities, which imply a lower gas mass fraction in the planets' compositions, could make in-situ formation an increasingly viable explanation (see e.g. Lee et al. 2014).

7.3. Stellar Composition & Planets

While Kepler-11 is slightly more metal-rich than the Sun, its relative elemental abundances have a similar trend with T_C to the solar abundance pattern. Under the Meléndez et al. (2009) hypothesis that the Sun's photospheric composition reflects its planet-forming history, we could interpret Kepler-11's abundance pattern as a signature of the formation of rocky planets. Such a chemical signature of terrestrial planet formation has also been revealed in Kepler-10 host star, showing the depletion of refractory materials when compared to its stellar twins (Liu et al. 2016). It is, however, somewhat dangerous to draw conclusions about the abundance pattern of an individual system, as many other factors can affect stellar abundances at the few-percent level, including galactic chemical evolution and circum-stellar disk physics (Gaidos 2015).

The relatively large uncertainty on the condensation temperature trend underscores the importance of galactic chemical evolution effects in particular. Although we have achieved very high-precision stellar abundance measurements, more work remains to be done on disentangling potential planet formation signatures from stellar age-dependent effects. For an individual system, even a solar twin with an age within a couple Gyr of the Sun, the uncertain effects of GCE make it extremely challenging to draw conclusions about the significance of the stellar abundance pattern in the context of planet formation. Fortunately, large-scale surveys like APOGEE and GAIA-ESO will provide the large sample sizes needed to refine abundance-age relations.

Regardless, it is surprising that a star that is nearly indistinguishable from the Sun even with our most advanced characterization methods is orbited by a planetary system that is so different from our own. This result continues the theme of exoplanet discoveries pointing towards a much larger variety of outcomes from the planet formation and evolution processes than was predicted even just a few years ago.

8. CONCLUSION

Using an extremely high-quality spectrum of the multi-planet host star Kepler-11, we have measured the stellar fundamental parameters and abundances to percent-level precision. We have also used a photodynamical model to fit the full *Kepler* lightcurve. Our planet orbital parameters agree with past publications. However, we find that the host star is younger than previously thought by a factor of ~ 3 , with a higher T_{eff} , $\log g$, and metallicity. Based on spectroscopic results, Kepler-11 and its planets are $\sim 30\%$ denser than previously reported. These results stand in tension with the lightcurve results.

The five inner planets of the Kepler-11 system are key members of the exoplanet mass-radius diagram as examples of the surprisingly low densities found in some planetary systems. The substantial revision of their properties reported here underscores the importance of detailed host star follow-up. As the community looks to exponentially increase the number of exoplanets with measured bulk densities through TESS and beyond, it is

critical to prioritize securing high-quality spectra of the host stars to enable the determination of precise host star properties.

This work was supported by a NASA Keck PI Data Award, administered by the NASA Exoplanet Science Institute. Data presented herein were obtained at the W. M. Keck Observatory from telescope time allocated to the National Aeronautics and Space Administration through the agency's scientific partnership with the California Institute of Technology and the University of California. The Observatory was made possible by the generous financial support of the W. M. Keck Foundation.

The authors wish to recognize and acknowledge the very significant cultural role and reverence that the summit of Mauna Kea has always had within the indigenous Hawaiian community. We are most fortunate to have the opportunity to conduct observations from this mountain.

M.B. is supported by a National Science Foundation Graduate Research Fellowship under Grant No. DGE-1144082. J.L.B. acknowledges support for this work from the NSF (grant number AST-1313119) and the Packard Foundation. J.M. thanks FAPESP (2012/24392-2). M.A., D.Y., and F.L. have been supported by the Australian Research Council (grants FL110100012, DP120100991 and FT140100554).

Facilities: Keck:I (HIRES), Kepler

REFERENCES

- Adibekyan, V. Z., Delgado Mena, E., Sousa, S. G., et al. 2012a, *A&A*, 547, A36
- Adibekyan, V. Z., Sousa, S. G., Santos, N. C., et al. 2012b, *A&A*, 545, A32
- Bedell, M., Meléndez, J., Bean, J. L., et al. 2014, *ApJ*, 795, 23
- Bensby, T., Feltzing, S., & Oey, M. S. 2014, *A&A*, 562, A71
- Bodenheimer, P., & Lissauer, J. J. 2014, *ApJ*, 791, 103
- Campante, T. L., Chaplin, W. J., Lund, M. N., et al. 2014, *ApJ*, 783, 123
- Carlos, M., Nissen, P. E., & Meléndez, J. 2016, *A&A*, 587, A100
- Chambers, J. E. 2010, *ApJ*, 724, 92
- Chiang, E., & Laughlin, G. 2013, *MNRAS*, 431, 3444
- dos Santos, L. A., Meléndez, J., do Nascimento, J.-D., et al. 2016, *A&A*, 592, A156
- Duncan, D. K. 1981, *ApJ*, 248, 651
- Epstein, C. R., Johnson, J. A., Dong, S., et al. 2010, *ApJ*, 709, 447
- Freitas, F. C., Meléndez, J., Bedell, M., et al. 2016, *A&A* submitted
- Gaidos, E. 2015, *ApJ*, 804, 40
- Hands, T. O., Alexander, R. D., & Dehnen, W. 2014, *MNRAS*, 445, 749
- Hinkel, N. R., Young, P. A., Pagano, M. D., et al. 2016, *ApJS*, 226, 4
- Howe, A. R., & Burrows, A. 2015, *ApJ*, 808, 150
- Ikoma, M., & Hori, Y. 2012, *ApJ*, 753, 66
- Kipping, D. M. 2014, *MNRAS*, 440, 2164
- Lee, E. J., Chiang, E., & Ormel, C. W. 2014, *ApJ*, 797, 95
- Lind, K., Asplund, M., & Barklem, P. S. 2009, *A&A*, 503, 541
- Lissauer, J. J., Fabrycky, D. C., Ford, E. B., et al. 2011, *Nature*, 470, 53

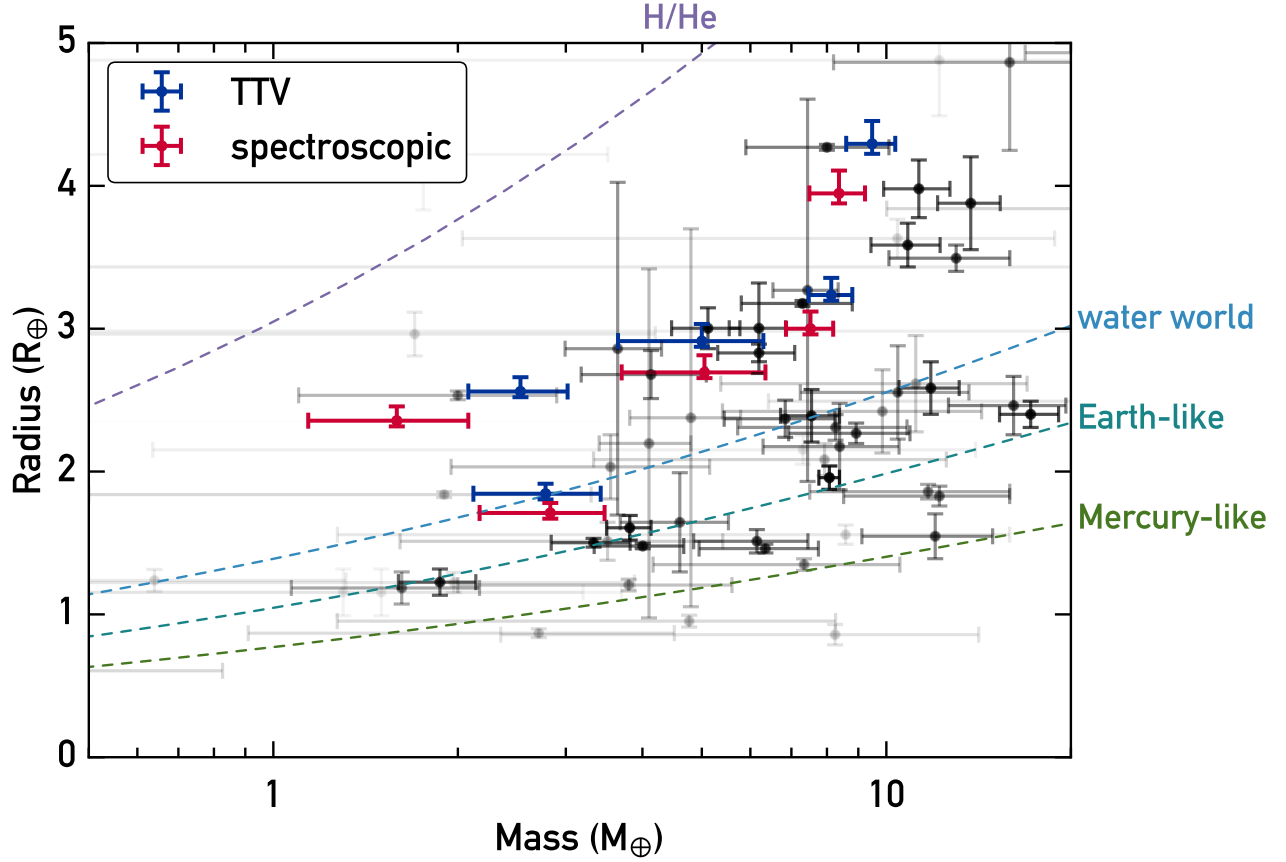


Figure 7. Exoplanets with measured masses and radii. Transparencies of the black points scale with the relative error on planet parameters. Kepler-11 a-e are plotted in **blue** (using the transit and TTV-derived parameters) and **red** (adjusted by the spectroscopic stellar parameters). Dashed lines show models of different compositions from Seager et al. (2007).

Lissauer, J. J., Jontof-Hutter, D., Rowe, J. F., et al. 2013, *ApJ*, 770, 131

Liu, F., Yong, D., Asplund, M., et al. 2016, *MNRAS*, 456, 2636

Lodders, K. 2003, *ApJ*, 591, 1220

Lopez, E. D., Fortney, J. J., & Miller, N. 2012, *ApJ*, 761, 59

Mahajan, N., & Wu, Y. 2014, *ApJ*, 795, 32

Meléndez, J., Asplund, M., Gustafsson, B., & Yong, D. 2009, *ApJL*, 704, L66

Meléndez, J., Bergemann, M., Cohen, J. G., et al. 2012, *A&A*, 543, A29

Meunier, N., Desort, M., & Lagrange, A.-M. 2010, *A&A*, 512, A39

Migaszwski, C., Słonina, M., & Goździewski, K. 2012, *MNRAS*, 427, 770

Morton, T. D. 2015, *isochrones: Stellar model grid package*, Astrophysics Source Code Library, , ascl:1503.010

Nissen, P. E. 2015, *A&A*, 579, A52

Oshagh, M., Santos, N. C., Ehrenreich, D., et al. 2014, *A&A*, 568, A99

Pál, A. 2012, *MNRAS*, 420, 1630

Radick, R. R., Lockwood, G. W., Skiff, B. A., & Baliunas, S. L. 1998, *ApJS*, 118, 239

Ramírez, I., Allende Prieto, C., & Lambert, D. L. 2007, *A&A*, 465, 271

Ramírez, I., Meléndez, J., Bean, J., et al. 2014, *A&A*, 572, A48

Reddy, B. E., Lambert, D. L., & Allende Prieto, C. 2006, *MNRAS*, 367, 1329

Rowe, J. F., Bryson, S. T., Marcy, G. W., et al. 2014, *ApJ*, 784, 45

Seager, S., Kuchner, M., Hier-Majumder, C. A., & Militzer, B. 2007, *ApJ*, 669, 1279

Skumanich, A. 1972, *ApJ*, 171, 565

Snedden, C. A. 1973, PhD thesis, THE UNIVERSITY OF TEXAS AT AUSTIN.

Spina, L., Meléndez, J., & Ramírez, I. 2016a, *A&A*, 585, A152

Spina, L., Meléndez, J., Karakas, A. I., et al. 2016b, *A&A*, 593, A125

- Ter Braak, C. J. F. 2005, Wageningen UR, Biometris, 010404, 556
- Teske, J. K., Ghezzi, L., Cunha, K., et al. 2015, ApJL, 801, L10
- Tucci Maia, M., Ramírez, I., Meléndez, J., et al. 2016, A&A, 590, A32
- Valenti, J. A., & Piskunov, N. 1996, A&AS, 118, 595
- Wang, J., Fischer, D. A., Horch, E. P., & Xie, J.-W. 2015, ApJ, 806, 248
- Weiss, L. M., & Marcy, G. W. 2014, ApJL, 783, L6
- Zacharias, N., Finch, C., Girard, T., et al. 2010, AJ, 139, 2184

Table 3. Line List and Measured Equivalent Widths.

Wavelength (Å)	Species	EP eV	$\log(gf)$ (dex)	Kepler-11 (mÅ)	Sun (mÅ)	HD1178 (mÅ)	HD10145 (mÅ)	HD16623 (mÅ)	HD20329 (mÅ)	HD21727 (mÅ)	HD21774 (mÅ)	HD28474 (mÅ)	HD176733 (mÅ)	HD191069 (mÅ)
5052.167	6	7.685	-1.24	35.2	33.5	32.7	27.9	21.4	29.4	26.6	41.6	17	27.4	36.7
6587.61	6	8.537	-1.05	16.9	15.2	17	12.2	9.8	11.4	11.7	20.3	6.2	10.8	17
7111.47	6	8.64	-1.07	13.2	11.3	12.1	15.1	9.6	12.3	10.9	16.6	36.7	10.2	14
7113.179	6	8.647	-0.76	25.3	22.4	23.2	20.3	13.8	17.9	19.5	33	11.3	18.2	24.3
7771.944	8	9.146	0.37	77.8	69.7	79.1	63.6	71	69.4	62.9	79.9	56.9	61.5	81.8
							:							

NOTE—Table 3 is published in its entirety in the machine-readable format. A portion is shown here for guidance regarding its form and content.

Table 4. Differential Abundances [X/H].

Element	T_e^1	N_{lines}	Kepler-11	HD1178	HD10145	HD16623	HD20329	HD21727	HD21774	HD28474	HD176733	HD191069
Cl	40	4	0.027 \pm 0.015	0.122 \pm 0.035	0.069 \pm 0.118	-0.204 \pm 0.082	0.053 \pm 0.079	0.029 \pm 0.061	0.182 \pm 0.041	-0.090 \pm 0.457	0.007 \pm 0.050	0.074 \pm 0.025
OI	180	3	0.058 \pm 0.012	0.179 \pm 0.077	0.083 \pm 0.021	-0.086 \pm 0.022	0.174 \pm 0.034	0.078 \pm 0.028	0.204 \pm 0.020	-0.269 \pm 0.022	0.048 \pm 0.028	0.145 \pm 0.019
NaI	958	4	0.045 \pm 0.017	-0.027 \pm 0.020	-0.117 \pm 0.047	-0.389 \pm 0.019	-0.035 \pm 0.037	-0.080 \pm 0.025	0.267 \pm 0.032	-0.558 \pm 0.054	-0.027 \pm 0.025	-0.010 \pm 0.022
MgI	1336	5	0.035 \pm 0.026	0.098 \pm 0.031	0.046 \pm 0.013	-0.228 \pm 0.049	0.047 \pm 0.116	0.058 \pm 0.059	0.258 \pm 0.043	-0.411 \pm 0.063	0.025 \pm 0.042	0.093 \pm 0.018
AlI	1653	2	0.061 \pm 0.008	0.176 \pm 0.018	0.035 \pm 0.005	-0.297 \pm 0.012	0.177 \pm 0.025	0.075 \pm 0.005	0.279 \pm 0.009	-0.469 \pm 0.007	0.042 \pm 0.005	0.114 \pm 0.011
SiI	1310	14	0.047 \pm 0.018	0.038 \pm 0.031	0.000 \pm 0.014	-0.285 \pm 0.028	0.042 \pm 0.046	0.022 \pm 0.028	0.245 \pm 0.021	-0.461 \pm 0.037	-0.004 \pm 0.019	0.040 \pm 0.012
SI	664	4	0.036 \pm 0.040	0.106 \pm 0.037	0.057 \pm 0.026	-0.249 \pm 0.063	0.034 \pm 0.086	0.021 \pm 0.025	0.235 \pm 0.025	-0.385 \pm 0.089	0.031 \pm 0.054	0.087 \pm 0.049
KI	1006	1	0.068 \pm 0.014	0.031 \pm 0.007	-0.039 \pm 0.008	-0.168 \pm 0.000	-0.025 \pm 0.006	-0.061 \pm 0.013	0.192 \pm 0.014	-0.355 \pm 0.006	-0.077 \pm 0.018	0.060 \pm 0.008
CaI	1517	11	0.066 \pm 0.018	0.072 \pm 0.028	0.016 \pm 0.015	-0.301 \pm 0.018	0.052 \pm 0.040	0.043 \pm 0.029	0.230 \pm 0.020	-0.494 \pm 0.020	-0.003 \pm 0.017	0.032 \pm 0.013
ScI	1659	4	0.086 \pm 0.037	0.096 \pm 0.032	0.027 \pm 0.027	-0.335 \pm 0.062	0.067 \pm 0.061	0.037 \pm 0.026	0.271 \pm 0.033	-0.368 \pm 0.079	0.005 \pm 0.043	0.070 \pm 0.014
ScII	1659	5	0.101 \pm 0.018	0.140 \pm 0.053	0.037 \pm 0.012	-0.288 \pm 0.035	0.144 \pm 0.051	0.107 \pm 0.047	0.316 \pm 0.023	-0.465 \pm 0.044	0.004 \pm 0.011	0.116 \pm 0.044
TiI	1582	18	0.065 \pm 0.021	0.113 \pm 0.024	0.046 \pm 0.044	-0.244 \pm 0.031	0.148 \pm 0.031	0.064 \pm 0.027	0.243 \pm 0.042	-0.451 \pm 0.024	0.009 \pm 0.021	0.080 \pm 0.020
TiII	1582	11	0.070 \pm 0.027	0.108 \pm 0.046	0.016 \pm 0.093	-0.229 \pm 0.049	0.117 \pm 0.031	0.025 \pm 0.100	0.275 \pm 0.044	-0.423 \pm 0.031	-0.007 \pm 0.027	0.101 \pm 0.038
VI	1429	9	0.078 \pm 0.017	0.078 \pm 0.018	-0.007 \pm 0.024	-0.323 \pm 0.029	0.097 \pm 0.089	0.043 \pm 0.027	0.275 \pm 0.023	-0.530 \pm 0.042	0.009 \pm 0.020	0.034 \pm 0.016
CrI	1296	10	0.047 \pm 0.020	0.017 \pm 0.022	0.008 \pm 0.058	-0.484 \pm 0.039	-0.065 \pm 0.028	0.012 \pm 0.017	0.272 \pm 0.035	-0.626 \pm 0.055	0.001 \pm 0.019	-0.023 \pm 0.016
CrII	1296	5	0.055 \pm 0.020	0.010 \pm 0.018	-0.012 \pm 0.050	-0.415 \pm 0.048	-0.073 \pm 0.017	0.014 \pm 0.028	0.243 \pm 0.028	-0.586 \pm 0.051	-0.025 \pm 0.024	-0.028 \pm 0.019
MnI	1158	8	0.060 \pm 0.025	-0.048 \pm 0.025	-0.071 \pm 0.030	-0.634 \pm 0.028	-0.183 \pm 0.018	-0.045 \pm 0.018	0.298 \pm 0.031	-0.778 \pm 0.058	-0.028 \pm 0.020	-0.084 \pm 0.017
FeI	1334	92	0.062 \pm 0.024	0.013 \pm 0.023	-0.016 \pm 0.050	-0.462 \pm 0.061	-0.093 \pm 0.022	0.005 \pm 0.069	0.252 \pm 0.079	-0.613 \pm 0.046	-0.018 \pm 0.028	-0.034 \pm 0.091
FeII	1334	17	0.064 \pm 0.020	0.011 \pm 0.047	-0.019 \pm 0.107	-0.461 \pm 0.075	-0.096 \pm 0.052	0.008 \pm 0.033	0.251 \pm 0.032	-0.617 \pm 0.071	-0.017 \pm 0.022	-0.030 \pm 0.036
CoI	1352	6	0.062 \pm 0.007	0.053 \pm 0.037	-0.026 \pm 0.023	-0.314 \pm 0.048	0.023 \pm 0.024	0.009 \pm 0.027	0.260 \pm 0.013	-0.499 \pm 0.038	-0.004 \pm 0.010	0.052 \pm 0.018
NiI	1353	20	0.066 \pm 0.021	0.010 \pm 0.024	-0.034 \pm 0.023	-0.443 \pm 0.025	-0.061 \pm 0.035	-0.001 \pm 0.040	0.278 \pm 0.029	-0.631 \pm 0.035	-0.012 \pm 0.039	-0.011 \pm 0.024
CuI	1037	4	0.080 \pm 0.011	0.075 \pm 0.032	-0.021 \pm 0.016	-0.472 \pm 0.054	0.000 \pm 0.011	-0.002 \pm 0.021	0.325 \pm 0.032	-0.630 \pm 0.090	0.053 \pm 0.034	0.056 \pm 0.021
ZnI	726	3	0.036 \pm 0.039	0.036 \pm 0.015	0.006 \pm 0.026	-0.315 \pm 0.048	0.056 \pm 0.031	-0.011 \pm 0.014	0.283 \pm 0.056	-0.539 \pm 0.087	-0.007 \pm 0.007	0.087 \pm 0.022
YII	1659	5	0.078 \pm 0.024	-0.025 \pm 0.008	-0.052 \pm 0.026	-0.579 \pm 0.031	-0.123 \pm 0.028	-0.047 \pm 0.012	0.228 \pm 0.013	-0.673 \pm 0.038	-0.051 \pm 0.026	-0.090 \pm 0.016
CH	40	3	0.054 \pm 0.007	-0.006 \pm 0.015	-0.070 \pm 0.021	-0.436 \pm 0.011	-0.199 \pm 0.019	-0.090 \pm 0.025	0.225 \pm 0.025	-0.620 \pm 0.012	-0.031 \pm 0.026	-0.003 \pm 0.027

¹ 50% condensation temperature for the element under protoplanetary disk conditions from Lodders (2003).